



available at www.sciencedirect.com



journal homepage: www.elsevier.com/locate/chnjc



Article

Facile fabrication and enhanced photocatalytic performance of visible light responsive UiO-66-NH₂/Ag₂CO₃ composite

Yun-Cai Zhou, Xue-Yan Xu, Peng Wang, Huifen Fu, Chen Zhao, Chong-Chen Wang *

Beijing Key Laboratory of Functional Materials for Building Structure and Environment Remediation, Beijing University of Civil Engineering and Architecture, Beijing 100044, China

ARTICLE INFO

Article history:

Received 1 May 2019

Accepted 26 June 2019

Published 5 December 2019

Keywords:

Metal-organic framework

Ag₂CO₃

Hexavalent chromium

Photocatalytic

Reaction mechanism

ABSTRACT

A series of UiO-66-NH₂/Ag₂CO₃ Z-scheme heterojunctions were prepared by a simple ion-exchange-solution method using UiO-66-NH₂ and semiconductor Ag₂CO₃ as precursors. The photocatalytic activities of UAC-X (UAC-20, 50, 100, 150, 200) Z-scheme heterojunctions toward the hexavalent chromium (Cr(VI)) reduction and UAC-100 toward oxidative degradation of four organic dyes like rhodamine B (RhB), methyl orange (MO), congo red (CR), and methylene blue (MB) under visible light irradiation were investigated. The effects of different pH (pH = 2, 3, 4, 6, 8), small organic acids (citric acid, tartaric acid, and oxalic acid), and foreign ions (ions in tap water and surface water) on Cr(VI) reduction were explored. The results revealed that the UAC-100 heterojunctions displayed more remarkable Cr(VI) reduction performance than the pristine UiO-66-NH₂ and Ag₂CO₃, resulting from the improved separation of photo-induced electrons and holes. The enhanced photocatalytic activity of UAC-100 was further confirmed by the photoluminescence measurement, electrochemical analysis, and active species trapping experiments. After four cycles' experiments, the photocatalytic Cr(VI) reduction efficiency over UAC-100 was still over 99%, which exhibited that UAC-100 had excellent reusability and stability. Finally, the corresponding photocatalytic reaction mechanism was proposed and tested.

© 2019, Dalian Institute of Chemical Physics, Chinese Academy of Sciences.

Published by Elsevier B.V. All rights reserved.

1. Introduction

As a consequence of economic development, population growth, urbanization, and infrastructural development, the ecological environment is undergoing great stress due to the discharge of wastewater containing heavy metals and organic pollutants [1]. Among various heavy metal ions, hexavalent chromium Cr(VI), as a mutagenic and carcinogenic pollutant, was widely spreading surface water and groundwater [2–4]. Up to now, some methods like ion exchange [5,6], adsorption [7],

membrane separation [8], electrocoagulation [9], and photocatalytic reduction [10] have been developed to remove Cr(VI) from wastewater. In all the above methods, photocatalytic reduction transformation from Cr(VI) to Cr(III) is an effective method to remove Cr(VI) from wastewater, considering that Cr(III) is less toxic and was removed as the form of Cr(OH)₃ in neutral or alkaline conditions [11]. Compared with traditional reduction methods like chemical reduction and electrochemical reduction [12], photocatalytic Cr(VI) reduction into Cr(III) exhibited the advantages like energy saving, high efficiency, and

* Corresponding author. Tel/Fax: +86-10-61209186; E-mail: wangchongchen@bucea.edu.cn

This work was supported by the National Natural Science Foundation of China (51878023, 51578034), Great Wall Scholars Training Program Project of Beijing Municipality Universities (CIT&TCD20180323), Project of Construction of Innovation Teams and Teacher Career Development for Universities and Colleges Under Beijing Municipality (IDHT20170508), Beijing Talent Project (2018A35), and BUCEA Post Graduate Innovation Project (PG2019039).

DOI: S1872-2067(19)63433-9 | http://www.sciencedirect.com/science/journal/18722067 | Chin. J. Catal., Vol. 40, No. 12, December 2019

free toxic by-product. Organic pollutants like organic dyes are not only toxic but also carcinogenic. Their chemical stability and hard degradation in nature will pose serious threats to human health and ecosystem sustainability. Numerous studies have shown that organic dye decomposition via a photocatalytic process is an efficient and practical solution [13–16]. In recent years, semiconductor photocatalysts have attracted wide attentions in solving global energy problems and environmental pollution [17–19]. Among various semiconductor photocatalysts, titanium dioxide (TiO_2) is widely used for pollutant removal with the aid of its advantages like toxicity free, high stability, and low cost [20–25]. However, the main disadvantage of TiO_2 is its only UV light response due to its large band gap, which greatly limits the use of sunlight (only 2%–3% of sunlight) [26]. At present, Ag_2CO_3 with a narrow band gap has been found to demonstrate remarkably photocatalytic activity in the visible light region [16,26–30]. Previous research focused on fabrication of Ag_2CO_3 onto different substrates as composite photocatalysts for water treatment, such as $\text{Ag}_2\text{CO}_3/\text{TiO}_2$ [26], $\text{Ag}_2\text{O}/\text{Ag}_2\text{CO}_3$ [27], and $\text{Ag}_2\text{CO}_3/\text{UiO-66}(\text{Zr})$ [16] along with $\text{GO-Ag}_2\text{CO}_3$ [31], which displayed the superior photocatalytic activity to Ag_2CO_3 but still suffered from serious photo-corrosion. Therefore, the improvements in both stability and photocatalytic activity of Ag_2CO_3 are the two main objectives to be achieved in future.

In the last two decades, metal-organic frameworks (MOFs) have been widely utilized as efficient photocatalysts to conduct CO_2 reduction [31–34], H_2 evolution [34–36], $\text{Cr}(\text{VI})$ reduction [2,13,17,37–41], and organic pollutant decomposition [10,15,16,42–44] because of the ultrahigh adsorption capacity and efficient light utilization ability [13,38,42,45]. However, the pristine MOFs as photocatalysts exhibit a large band gap and can only be degraded by ultraviolet light, which will greatly reduce the utilization of solar energy. Up to now, numerous studies have focused on immobilizing other photocatalytically active semiconductors on MOFs substrates to extend the photo-responsive region to the visible region. For example, Ag_2CO_3 was attached to UiO-66 to construct a binary composite for visible-light-driven degradation of organic dyes [16]. Metal free $\text{g-C}_3\text{N}_4$ was encapsulated on BUC-21 for photocatalytic reduction of $\text{Cr}(\text{VI})$ under simulated sunlight irradiation [39]. As well, MIL-53(Al) was decorated with $\text{g-C}_3\text{N}_4$ for enhanced photocatalytic rhodamine B (RhB) decomposition under visible-light irradiation [46]. These studies demonstrated that MOFs/semiconductors composites exhibited increasing light utilization efficiency than the individual MOFs. Hence, MOFs can act as a perfect substrate to load a variety of semiconductor materials to form heterojunction for potential applications in water treatment. Among all MOF materials, UiO-66 as a zirconium-based three-dimensional MOF not only has the advantages of other MOFs, but also has excellent thermal stability and chemical stability [47,48]. In 2015, Wu et al. [16] reported that UiO-66 (Zr) and Ag_2CO_3 are combined to enhance the visible light catalytic degradation of RhB. Zhang et al. [49] constructed the $\text{Ag}_3\text{PO}_4/\text{UiO-66}$ heterojunction for efficient visible light degradation of RhB. Our research group found that UiO-66- $\text{NH}_2/\text{Ag}_3\text{PO}_4$ and UiO-66- $\text{NH}_2/\text{Ag}_2\text{CO}_3$ composites ex-

hibited effective capture and visible-triggered release toward sulfonamides due to the formation and split between Ag^+ and $-\text{NH}_2$ group [50,51]. Up to now, there has been no report on the efficiently photocatalytic $\text{Cr}(\text{VI})$ reduction over UiO-66- $\text{NH}_2/\text{Ag}_2\text{CO}_3$ composites under visible light illumination. With this paper, the UiO-66- $\text{NH}_2/\text{Ag}_2\text{CO}_3$ Z-scheme heterojunction (UAC-X Z-scheme heterojunction) is used to achieve photocatalytic $\text{Cr}(\text{VI})$ reduction under visible light irradiation. In addition, the stability of the UiO-66- $\text{NH}_2/\text{Ag}_2\text{CO}_3$ heterojunction was investigated, and the photocatalytic mechanism was proposed and tested.

2. Experimental

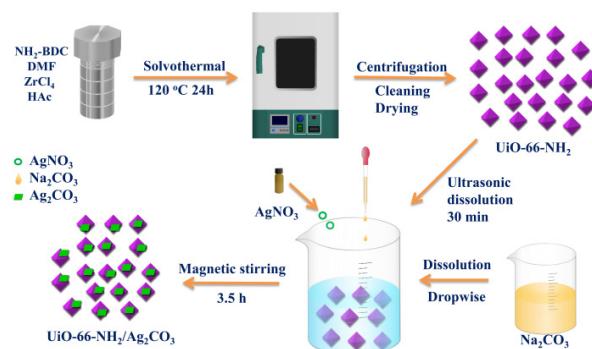
2.1. Materials and characterization

All materials and reagents were commercially available and used directly without further purification. The characterization methods are listed in the Supporting Information.

2.2. Preparation of UiO-66- $\text{NH}_2/\text{Ag}_2\text{CO}_3$ composites

The UiO-66- NH_2 was hydrothermally synthesized as described in a previous report with slight modification [35]. Briefly, 2-aminoterephthalic acid ($\text{NH}_2\text{-BDC}$) (4.5 mmol, 0.81 g) was completely dissolved in N,N' -dimethylformamide (DMF, 40 mL) by ultrasound for ca. 10 min. Then, ZrCl_4 (4.5 mmol, 1.05 g) and acetic acid (HAc, 17 mL) were added to this solution. All the above processes were carried out in a 100 mL Teflon-lined stainless-steel autoclave. HAc was added to tune the morphology of UiO-66- NH_2 . The autoclave was placed in a drying oven and heated at 120 °C for 24 h. After cooling to room temperature, the product was centrifuged and cleaned several times with ultra-pure water. The prepared UiO-66- NH_2 was dried at 60 °C in a drying oven before use.

UAC-X composites (UAC-20, 50, 100, 150, 200) were fabricated by a simple ion-exchange-solution method with a small modification [16,50,51], as illustrated in Scheme 1. Taking UAC-100 (the weight ratio of UiO-66- NH_2 and Ag_2CO_3 being 1:1) for an example, the Na_2CO_3 aqueous solution (10 mL, 0.030 mol/L) was added dropwise into the suspension (100 mL) of UiO-66- NH_2 (1000 mg/L) and AgNO_3 (0.006 mol/L). The mixture was stirred vigorously with a magnetic stirrer for 3.5 h.



Scheme 1. Illustration of the fabrication of UiO-66- $\text{NH}_2/\text{Ag}_2\text{CO}_3$ (UAC-X) composites.

The precipitates were separated from the solution via filtration and washed with ultra-pure water and EtOH several times. The other UiO-66-NH₂/Ag₂CO₃ (UAC-X) composite samples were fabricated similarly to UAC-100. The weight proportions of UiO-66-NH₂ and AgNO₃ in UAC-20, UAC-50, UAC-150 and UAC-200 were 0.2:1, 0.5:1, 1.5:1, and 2:1, respectively. For the sake of comparison, Ag₂CO₃ particles were also synthesized following the same method as UAC-100 except without adding UiO-66-NH₂.

2.3. Adsorption-photocatalysis experiment

The photocatalytic performance of UAC-X composites toward Cr(VI) reduction and organic pollutant degradation was investigated under visible light irradiation at ambient temperature. The photocatalytic Cr(VI) reduction experiment was carried out in a 50 mL quartz glass vessel containing 10 mg UAC-X composites (or individual UiO-66-NH₂ and Ag₂CO₃) and 40 mL Cr(VI) solution (10 mg/L). It is worth noting that the pH of Cr(VI) solution was adjusted to 2.0 with H₂SO₄ solution. The suspension was first magnetically stirred in the dark for 45 min to achieve adsorption-desorption equilibrium. Afterwards, the Cr(VI) solution was irradiated with 5.00 W LED (PCX50A, Beijing perfect light technology Co., LTD) for 60 min, and the spectrum of light source (longer than 420 nm) is shown in Fig. S1. At specific time interval, 1.5 mL liquor was drawn and filtered through 0.45 μ m syringe filter for analysis. The residual Cr(VI) was determined by a diphenylcarbazide (DPC) method via an

Auto Analyzer 3 (Seal, Germany). The operation flow and video of Auto Analyzer 3 are shown in Fig. S2. Blank experiments were also carried out under the identical conditions with no photocatalyst addition.

3. Results and discussion

3.1. Characterization

The FTIR spectra of Ag₂CO₃, UiO-66-NH₂, and UAC-X composites (Fig. 1a) revealed that the adsorption peaks at 1581.92 and 1382.09 cm⁻¹ were assigned to the carboxylic functional groups in the BDC-NH₂ ligands, and the peaks between 600–800 cm⁻¹ were ascribed to Zr–O₂ as vertical and horizontal mode scaling [52,53]. The peaks at 1374.62 and 803.06 cm⁻¹ were attributed to the characteristic peaks for CO₃²⁻ [46]. The characteristic adsorption peaks of UiO-66-NH₂ at 1581.92, 1382.09, and 600–800 cm⁻¹ decreased with the decrease of UiO-66-NH₂ contents. On the contrary, with the decrease of UiO-66-NH₂ contents, the characteristic peaks of Ag₂CO₃ at 1374.62 and 803.06 cm⁻¹ increased obviously [51].

The powder XRD patterns (Fig. 1b) of the as-synthesized UiO-66-NH₂ are in consistent with the reported ones [46], indicating that UiO-66-NH₂ was successfully prepared. All the diffraction peaks of pristine Ag₂CO₃ matched well with the standard pattern (JCPDS card No. 97-000-8011) (Fig. S3) of Ag₂CO₃ with monoclinic structure [50]. It is worth noting that the characteristic peaks of both UiO-66-NH₂ and Ag₂CO₃ could be

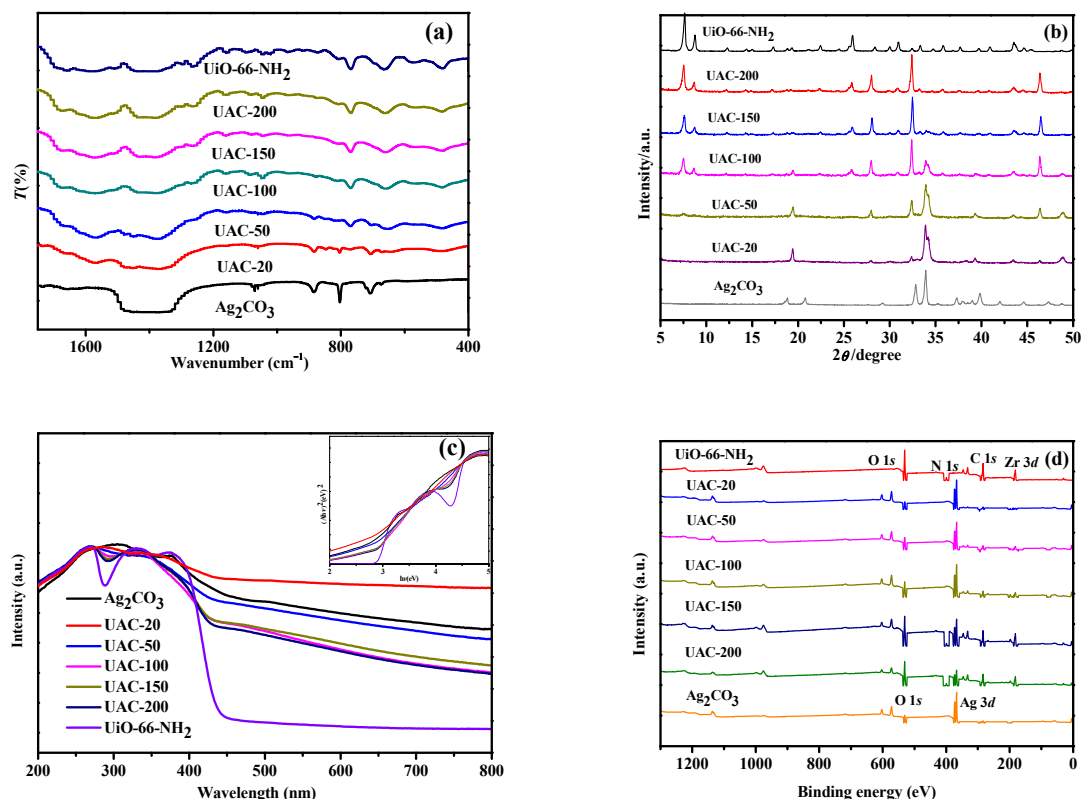


Fig. 1. (a) FTIR spectra, (b) PXRD patterns, (c) UV-vis DRS and E_g plot (inset), and (d) XPS spectra of Ag₂CO₃, UiO-66-NH₂, and the UAC-X composites.

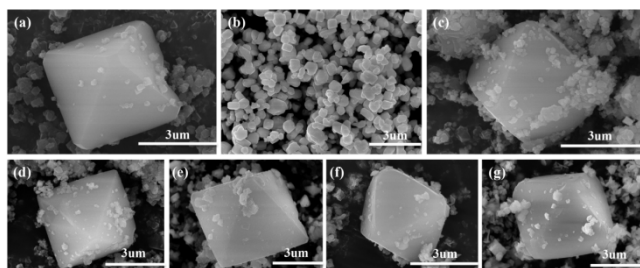


Fig. 2. SEM images of (a) UiO-66-NH₂, (b) Ag₂CO₃, (c) UAC-20, (d) UAC-50, (e) UAC-100, (f) UAC-150, and (g) UAC-200.

detected in UAC-100. The peaks of Ag₂CO₃ vanished gradually as the small Ag₂CO₃ content decreased in UAC-150 and UAC-200. Similarly, the characteristic peaks of UiO-66-NH₂ could be detectable in both UAC-20 and UAC-50 [51].

The UV-vis diffuse reflectance spectra (UV-vis DRS) of Ag₂CO₃, UiO-66-NH₂, and UAC-X composites are displayed in Fig. 1c. The peak of pristine UiO-66-NH₂ is a wide peak between 200 and 430 nm, which is consistent with the peak previously reported [39,40]. The light absorption region of UAC-X is almost the same as that of Ag₂CO₃, and their E_g values are in the range of 2.25–2.95 (inset in Fig. 1c), indicating that both UiO-66-NH₂ and UAC-X composites can be excited by visible light [40].

The successful fabrication of UAC-X composites was further confirmed by XPS determination (Fig. 1d). The XPS spectrum revealed that the Ag 3d in UAC-X displayed a slight shift to higher binding energy compared to the pristine Ag₂CO₃, which may be due to the synergy between UiO-66-NH₂ substrate and Ag₂CO₃ [50,51].

The SEM and TEM images could be used to specifically un-

derstand the morphology of Ag₂CO₃, UiO-66-NH₂, and UAC-X composites. It was observed by SEM (Fig. 2a) that the individual UiO-66-NH₂ particles were standard regular octahedrons of different sizes ranging from 200 nm to 3500 nm, in which the UiO-66-NH₂ with small particle size exhibited regular octahedrons shape (as shown in Fig. S4). Ag₂CO₃ presents irregular cubic structure [27] with particle size distribution between 100 and 400 nm. Both SEM (Fig. 2) and TEM (Fig. S5) images illustrated that Ag₂CO₃ nanoparticles are adhered to the surface of UiO-66-NH₂. The HRTEM image of UAC-100 (Fig. S6) reveals that the lattice spacing of 0.261 nm corresponds to the (130) facet of Ag₂CO₃, further indicating the intimate contact between UiO-66-NH₂ and Ag₂CO₃ [51]. The content of octahedral UiO-66-NH₂ in UAC-X composites affected the adhesion state of Ag₂CO₃ on UiO-66-NH₂. The element distribution results of UAC-100 are depicted in Fig. S7, in which the Ag, Zr, C, N, and O elements are evenly distributed over the composite, further indicating that Ag₂CO₃ is successfully loaded onto the UiO-66-NH₂ material. In the XPS spectrum of UAC-100 (Fig. 3), the combination between Ag₂CO₃ and UiO-66-NH₂ was affirmed by the shift of binding energies of Zr, Ag, C, N, and O, which was deeply discussed in our previous reports [50,51].

3.2. Photocatalytic performance

3.2.1. Photocatalytic Cr(VI) reduction

In order to explore the photocatalytic performance of Ag₂CO₃, UiO-66-NH₂ and UAC-X composites, the Cr(VI) reduction efficiency at pH = 2 was investigated. As shown in Fig. 4a, Cr(VI) can not be reduced to Cr(III) without adding photocatalyst both in dark and under the irradiation of visible light. In the experiment, Cr(VI) was first adsorbed in the dark for 45 min,

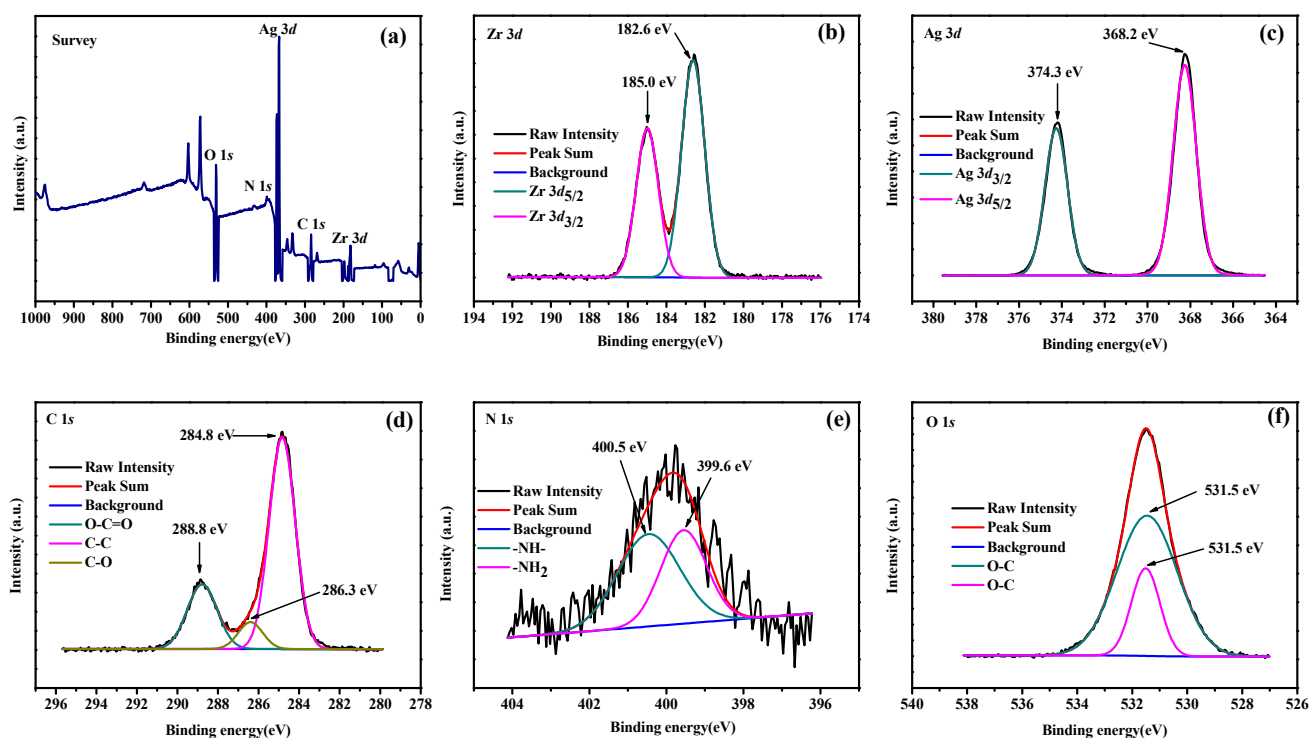


Fig. 3. (a) XPS survey, (b) Zr 3d, (c) Ag 3d, (d) C 1s, (e) N 1s, and (f) O 1s spectra of UAC-100 composite.

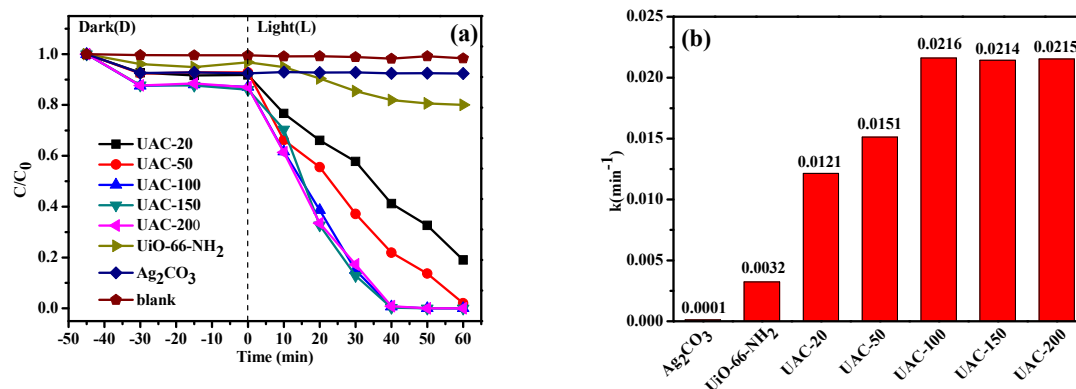


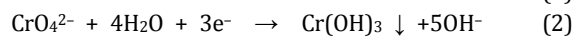
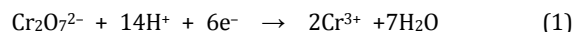
Fig. 4. (a) The adsorption and photocatalytic performance and (b) the photocatalytic reduction rates (k values) of Ag_2CO_3 , UiO-66-NH_2 , and UAC-X composites toward Cr(VI) reduction. Conditions: $\text{Cr(VI)} = 10 \text{ mg/L}$, volume 40 mL , $\text{pH} = 2$, photocatalyst dosage 10 mg .

and the adsorptive removal efficiencies of Ag_2CO_3 , UiO-66-NH_2 , and UAC-X composites toward Cr(VI) ranged from 3% to 14%. As shown in Fig. 4a and Table 1, under the identical conditions, the photocatalytic performance of the UAC-X composites for Cr(VI) reduction is better than those of pristine UiO-66-NH_2 or Ag_2CO_3 . UAC-100 , UAC-150 , and UAC-200 can achieve 100% Cr(VI) reduction within 50 min, which are higher than the reduction efficiencies of UAC-20 (68%), UAC-50 (86%), UiO-66-NH_2 (19%), and Ag_2CO_3 (8%). Specifically, the pseudo-first-order model of UAC-X for Cr(VI) reduction further proves that UAC-100 achieved faster efficient reduction rate (k value), as shown in Fig. 4b. Comparing with the UAC-20 and UAC-50 , UAC-100 exhibited more outstanding photocatalytic performance toward Cr(VI) reduction under the identical conditions, which may be related to the larger specific surface area of UAC-100 than both UAC-20 and UAC-50 (Table S1). Both the positive zeta potential (Fig. S8c) and larger surface area facilitate the adsorption toward $\text{Cr}_2\text{O}_7^{2-}$ for further photocatalysis [29,37]. As well, the appropriate introduction of Ag_2CO_3 into UiO-66-NH_2 will improve the charge transfer over the composite interfaces under visible light irradiation [54]. However, excessive UiO-66-NH_2 in the UAC-X may suppress the valid heterogeneous interfaces, which is not conducive to the transfer of charge carriers [55]. In view of economic and cost savings, UAC-100 can achieve the desired effect under the same conditions using less UiO-66-NH_2 compared to UAC-150 and UAC-200 . Therefore, the UAC-100 was selected to conduct follow-up experiments for deep understanding toward its perfor-

mance.

3.2.1.1. Effect of initial pH value on Cr(VI) reduction

The initial pH value of Cr(VI) has a great influence on its reduction effect [56]. In this study, the effects of different pH values ($\text{pH} = 2, 3, 4, 6, 8$) on the Cr(VI) reduction were investigated using UAC-100 as photocatalyst. As illustrated in Fig. 5a, the lower pH resulted in a better photocatalytic efficiency and rate. Especially, the highest photocatalytic Cr(VI) reduction efficiency (99.0% within 40 min and 100.0% within 50 min) was accomplished at $\text{pH} = 2.0$. It is well known that hexavalent chromium exists in the form of $\text{Cr}_2\text{O}_7^{2-}$ at low pH [37]. At this lower pH, the higher degree of protonation on the catalyst surface facilitates the adsorptive interactions with $\text{Cr}_2\text{O}_7^{2-}$ ions, and the abundant H^+ also promotes the transformation from Cr(VI) to Cr(III) , as listed in Eq. (1) [56]. Under alkaline conditions, the composite photocatalysts displayed negative zeta potentials (as illustrated in Fig. S8), which would decline the adsorptive interactions toward anionic CrO_4^{2-} . As well, the Cr(VI) reduction reaction under alkaline surroundings follows Eq. (2) [17]. However, the formed Cr(OH)_3 can cover the active sites over the catalyst surface, resulting into declined photocatalytic efficiency.



3.2.1.2. Effects of foreign ions on Cr(VI) reduction

In order to explore the influences of foreign ions on the photocatalytic Cr(VI) reduction activity, UAC-100 catalyst was used to treat a Cr(VI) solution ($\text{pH} = 2$) prepared with real lake water collected from the Ming Lake and tap water of Daxing campus, BUCEA (the quality parameters of lake water and tap water are shown in Table S2). As shown in Fig. 5b, it was found that the Cr(VI) reduction efficiency declined from 100% to 46% in 60 min, indicating that the Cr(VI) reduction over UAC-100 was inhibited by the inorganic ions in tap water [44]. It is worth noting that the Cr(VI) reduction efficiency in lake water was higher (76%, 60 min) than that in tap water because the organic matters in the lake water could consume the holes to facilitate the separation of photo-induced electrons and holes

Table 1

Photocatalytic Cr(VI) reduction efficiencies (%) of different photocatalysts.

Catalyst	Efficiency (%)		
	40 min	50 min	60 min
UAC-20	59	68	81
UAC-50	78	86	98
UAC-100	99	100	100
UAC-150	99	100	100
UAC-200	99	100	100
UiO-66-NH_2	18	19	20
Ag_2CO_3	8	8	8

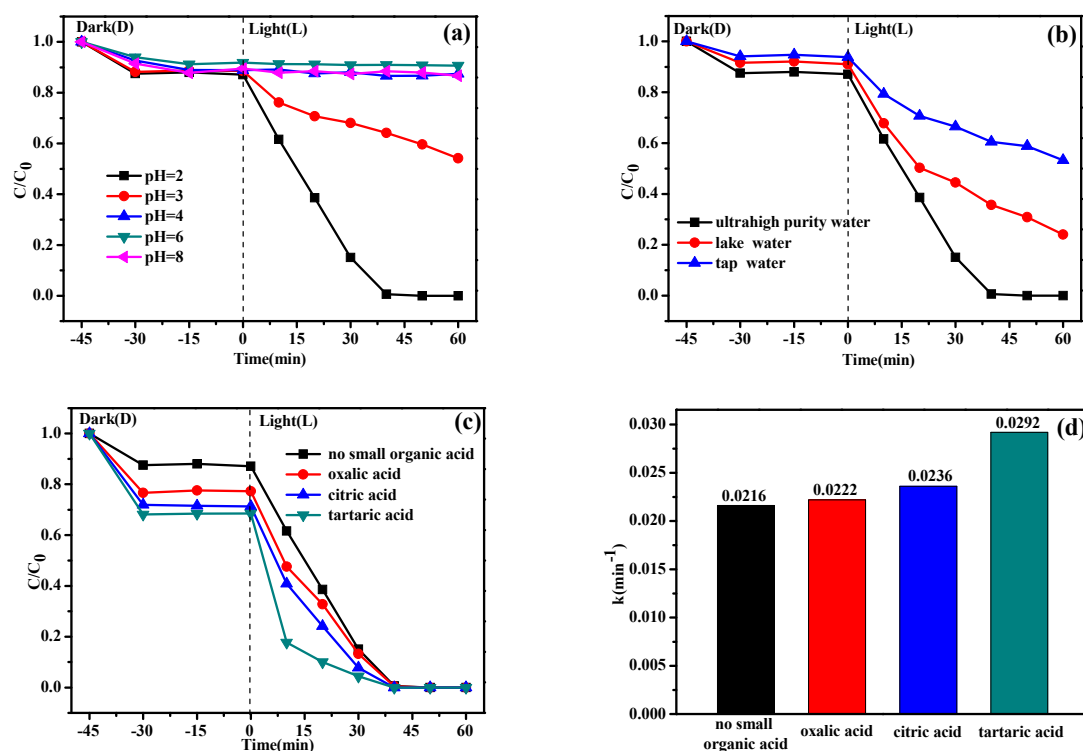


Fig. 5. (a) Photocatalytic Cr(VI) reduction efficiencies with UAC-100 as photocatalyst at different pH values; (b) Effect of Cr(VI) solution prepared from tap water and lake water on reduction of Cr(VI); (c) Effect of different small organic acids on the Cr(VI) reduction; (d) Photocatalytic Cr(VI) reduction rates (k values) in the presence of different small organic compounds. Conditions: UAC-100 = 10 mg, Cr(VI) = 10 mg/L, 40 mL, pH = 2.0, small organic acid dosage = 0.1 mmol/L.

[57]. It can be concluded that the organic matters in the reaction system can enhance the photocatalytic Cr(VI) reduction performance.

3.2.1.3. Effects of small organic acids on Cr(VI) reduction

Photo-induced electron-hole pairs can be produced upon visible light irradiation. The consumption of holes (h^+) will accelerate the charge separation of photo-induced electron-hole pairs, resulting in excellent Cr(VI) reduction efficiency. In order to test the effect of small organic acids as hole scavengers on the Cr(VI) reduction efficiency, some organic compounds such as citric acid, tartaric acid, and oxalic acid were selected as hole scavengers at pH = 2.0. As shown in Fig. 5c and 5d, the participation of these small organic acids can improve the photocatalytic Cr(VI) reduction activity, because the organic matters consume the holes generated over the UAC-100 photocatalyst upon light irradiation. It is worth noting that the presence of small organic compounds can improve the photocatalytic reaction rate of Cr(VI) reduction, which may be related to the number of α -hydroxyl carboxylate functional groups (zero, one, and two α -hydroxyl groups in oxalic acid, citric acid, and tartaric acid, respectively) [12,39].

3.2.2. Photocatalytic degradation activities toward different organic dyes

Different organic dyes like rhodamine B (RhB), methyl orange (MO), congo red (CR), and methylene blue (MB) were

selected to investigate the degradation performance of UAC-100. UAC-100 displayed negative zeta potential when pH was higher than 3.3 (pH_{PZC}) (Fig. S8), which favored the adsorption toward cationic organic dyes. During the adsorption process in dark, UAC-100 displayed different adsorption performance toward cationic RhB and MB along with anionic MO and CR. It can be found that UAC-100 exhibits the best adsorption ability toward MB due to electrostatic interaction. However, the size of RhB (1.56 nm × 1.35 nm × 0.42 nm) is slightly larger than MB (1.38 nm × 0.64 nm × 0.21 nm), and the pore size of UAC-100 is ca. 0.6 nm (Fig. S9), which leads to the poorer adsorption performance toward RhB than that toward MB. With the aid of weak interaction between Ag^+ in UAC-100 and the $-NH_2$ group [50,51,58], UAC-100 displays noticeable adsorption toward CR with the adsorption efficiency of 28%. And, the electrostatic repulsion between UAC-100 and MO leads to nearly no adsorptive interactions. Upon the light irradiation, 96% MB and 81% CR can be decomposed within 60 min, while 90% MO and 85% RhB can be degraded up to 90 min. It can be concluded that UAC-100 can achieve the photocatalytic degradation toward organic pollutants like stable organic dyes.

3.2.2.1. Identification of active species

In order to further understand the intrinsic reactions, some measures were taken to explore the active species that play a role in the process of photocatalytic. Specifically, EDTA-2Na (0.2 mmol/L), benzoquinone (BQ, 0.2 mmol/L), and isopropyl

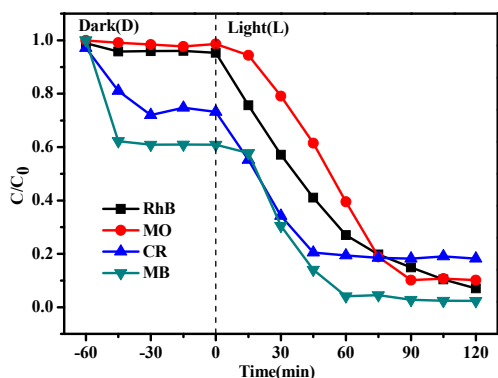


Fig. 6. The photocatalytic degradation performance of UAC-100 toward different organic dyes (RhB, MO, CR, MB). Reaction conditions: 10 mg UAC-100, 40 mL of RhB (10 mg/L) or MO (10 mg/L) or CR (50 mg/L) or MB (10 mg/L).

alcohol (IPA, 0.6 mmol/L) were added to the solution to capture h^+ , $\bullet O_2^-$, and $\bullet HO$, respectively. It has been pointed out that $\bullet HO$ and $\bullet O_2^-$ are important photoactive substances that can degrade pollutants [16,27,31,44,59]. As shown in Fig. 7a, the degradation of MB by UAC-100 was significantly inhibited after the addition of different sacrificial agents, indicating that all the h^+ , $\bullet HO$, and $\bullet O_2^-$ can achieve the oxidative degradation toward the organic dyes under visible light. The electron spin resonance (ESR) determination can also prove the existence of $\bullet O_2^-$ and $\bullet HO$, as shown in Fig. 7b and 7c.

3.2.3. Photocatalytic performance toward Cr(VI) and MB in their matrix

It is well known that heavy metals like Cr(VI) often existed with various organic pollutants in industrial wastewater. In this experiment, the photocatalytic activity of UAC-100 for simultaneous Cr(VI) reduction and organic dye degradation at pH = 2 was investigated. As shown in Fig. 8, in the mono-system of Cr(VI) and MB, UAC-100 could remove 100% Cr(VI) and 96% MB after 60 min illumination, respectively. However, in the Cr(VI) and MB matrix, only 79% Cr(VI) and 78% MB were removed under visible light for 60 min. The removal efficiency of both Cr(VI) and MB over UAC-100 in the mixed system became slower than that of the mono-component, possibly due to the

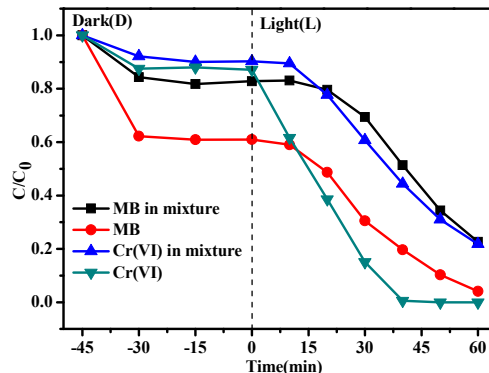


Fig. 8. Photocatalytic Cr(VI) reduction and MB degradation efficiencies in their single systems and in their matrix with UAC-100 as photocatalyst. Reaction conditions: 10 mg UAC-100, 40 mL of Cr(VI) (10 mg/L) and MB (10 mg/L), pH = 2.0.

competition of $\bullet O_2^-$ between Cr(VI) and MB (detailed discussion can be found in Section 3.2.5).

3.2.4. Reusability and stability of UAC-100

It is important to explore the reusability and stability of the UAC-X composites for practical application, which was performed by accomplishing repeated cycles under determinate reaction conditions. As illustrated in Fig. 9a, UAC-100 shows the superior photocatalytic Cr(VI) reduction activity of more than 99% after four cycles. The PXRD patterns (Fig. 9b) of the recovered UAC-100 after four cycles matched well with the original ones, implying that UAC-100 has excellent reusability and stability. In addition, there is no obvious change in the octahedron shape of UiO-66-NH₂ after four runs (Fig. S10), indicating that the composite material can be reused without obvious erosion and deterioration. The XPS spectrum of UAC-100 after the photocatalytic reaction further demonstrates the integrity of UAC-100 (as shown in Fig. S11), which has only a small amount of Cr(III) formed by Cr(VI) reduction (the binding energy of 573.3 eV corresponds to Cr 2p_{3/2} orbital of Cr(III)) [60].

It should be noted that 99% Cr(VI) reduction can be achieved after four cycles of visible light irradiation for 50 min over UAC-100 without adding any hole scavenger to promote the reaction. Compared to some typical metal-organic frame-

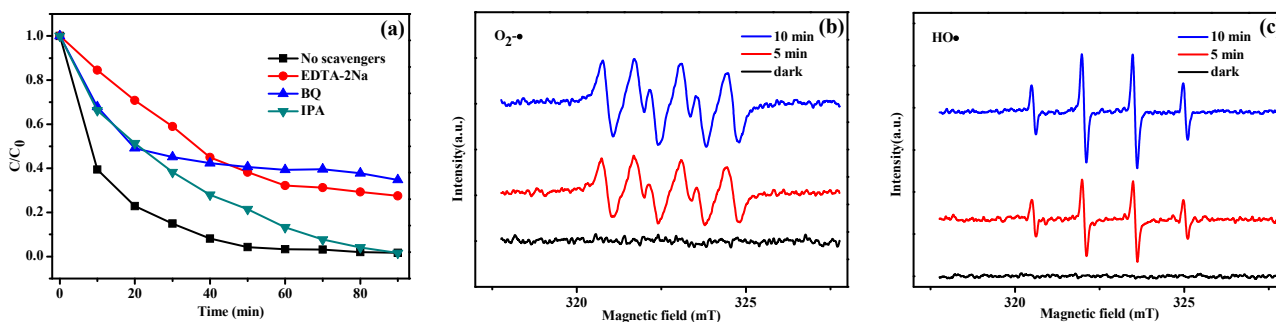


Fig. 7. (a) The effects of different scavengers on the degradation of MB in the presence of UAC-100 under visible light irradiation. Conditions: MB = 10 mg/L, 40 mL, UAC-100 = 10 mg. ESR spectra of radical adducts trapped by DMPO- $\bullet O_2^-$ (b) and DMPO- $\bullet HO$ (c) over UAC-100 under visible light irradiation.

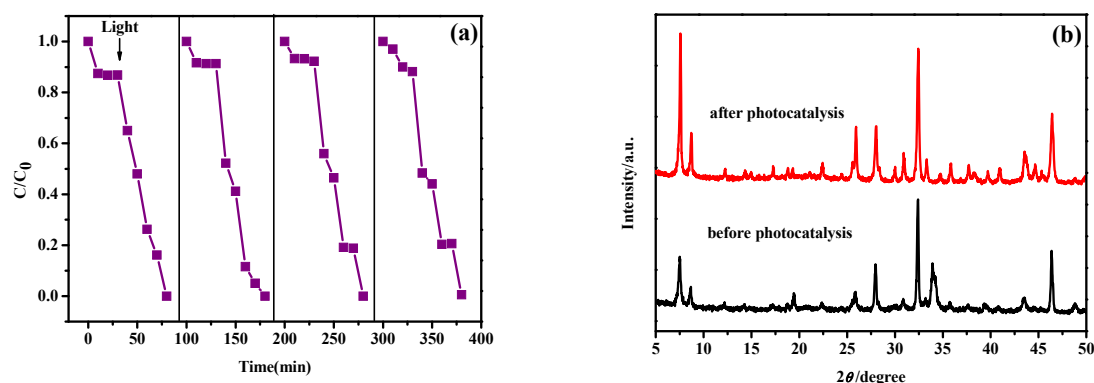


Fig. 9. (a) The reusability of UAC-100 under visible light conditions (photocatalytic reduction of $Cr(VI)$) and dark conditions (adsorption of $Cr_2O_7^{2-}$); (b) Comparison of PXRD before and after four cycles of photocatalytic $Cr(VI)$ reduction solution by UAC-100 composite.

works or their composites, UAC-100 exhibits an excellent ability to reduce $Cr(VI)$ after 50 min irradiation under 5.00 W LED, as illustrated in Table 2. It is found that UAC-100 displayed superior photocatalytic $Cr(VI)$ performance among the reported photocatalysts in Table 2, considering the photocatalyst dosage, initial $Cr(VI)$ concentration, solution volume, cycle times, and light source.

3.2.5. Photocatalytic reaction mechanism

The photoluminescence technique (PL) was used to evaluate the separation efficiency of carrier charges in catalytic process of the composites [41,64,65]. Generally, the higher fluorescence emission intensity implies the faster recombination of photo-induced electrons and holes, resulting in a decrease of the photocatalytic performance. $UiO-66-NH_2$, Ag_2CO_3 , and UAC-100 are excited to produce the excitation peak centered at 350 nm. However, UAC-100 displayed a slight blue-shift relative to $UiO-66-NH_2$ and Ag_2CO_3 , in which the emission peaks of $UiO-66-NH_2$, Ag_2CO_3 , and UAC-100 are centered at 542, 540, and 540 nm, respectively. It can be seen from Fig. 10a that the fluorescence intensity of UAC-100 is significantly weaker than that of $UiO-66-NH_2$ and Ag_2CO_3 , indicating that photo-induced electrons and holes over UAC-100 are effectively separated. This can also be confirmed by the transient photocurrent response value [64,65]. The photo-electrode prepared from UAC-100 can generate reversible and stable photocurrent under visible light illumination, and the photocurrent intensity of UAC-100 is obviously higher than that of $UiO-66-NH_2$ and

Ag_2CO_3 (Fig. S12). The transient photocurrent responses further prove that the separation efficiency of photo-induced electron and hole pairs over the composites is improved significantly.

Electrochemical impedance spectroscopy (EIS) of $UiO-66-NH_2$, Ag_2CO_3 , and UAC-100 was performed for analysis of charge transfer and recombination, in which the diameter of the arc on an EIS Nyquist diagram is equal to the charge transfer resistance occurred at the semiconductor-electrolyte interface [66]. The smaller Nyquist radius implied the smaller corresponding charge transfer resistance. As depicted in Fig. 10b, the arc radius of the UAC-100 composite is much smaller than that of $UiO-66-NH_2$ and Ag_2CO_3 , indicating that the photo-induced holes and electrons over the UAC-100 are effectively separated to accomplish the higher photocatalytic activity.

The Mott-Schottky curves of Ag_2CO_3 and $UiO-66-NH_2$ (Fig. 10c and 10d) illustrate negative and positive correction between C^2 value and potential value, implying that Ag_2CO_3 and $UiO-66-NH_2$ displayed the typical behavior of p-type semiconductor and n-type semiconductor, respectively [67]. Compared with the pristine Ag_2CO_3 and $UiO-66-NH_2$, the enhanced photocatalytic activity of UAC-X composites may be assigned to the p-n junction formed between the n-type $UiO-66-NH_2$ and the p-type Ag_2CO_3 semiconductor. It can be roughly inferred from the Mott-Schottky spectrogram that the flat band potentials (E_{FB}) of $UiO-66-NH_2$ and Ag_2CO_3 are *ca.* -1.29 and 0.51 eV vs $Ag/AgCl$ electrode, respectively. According to the band gap value (E_g ($UiO-66-NH_2$) = 2.92 eV, E_g (Ag_2CO_3) = 2.64 eV) and

Table 2

Performance of some typical metal-organic frameworks (or their composites) as photocatalysts for the reduction of $Cr(VI)$ under visible light irradiation.

Photocatalyst/ Amount (mg)	$Cr(VI)$ concentration (mg/L)/Solution volume (mL)/pH	Time/ (min)	1st cycle reduction efficiency (%)	Times/Last cycle re- duction efficiency (%)	Light source	Ref.
MIL-101(Fe)/20	8/40/2.0	60	100	NA	300W Xe Lamp	[37]
NH_2 -MIL-88B/20	8/40/2.0	50	100	4/100	300W Xe Lamp	[37]
$UiO-66-NH_2$ /20	10/40/2.0	80	97	3/97	300W Xe Lamp	[40,61]
BUC-21/g- C_3N_4 /50	10/200/2.0	120	<i>ca.</i> 97	5/ <i>ca.</i> 89	500 W Xe Lamp	[39]
$Pd@UiO-66(NH_2)$ /20	10/40/2.0	90	100	3/ <i>ca.</i> 98	300 W Xe Lamp	[62]
RGO- $UiO-66(NH_2)$ /20	10/40/2.0	100	100	3/ <i>ca.</i> 100	300 W Xe Lamp	[63]
$UiO-66-NH_2/Ag_2CO_3$ /10	10/40/2.0	50	100	4/99	5.00 W LED	this work

Notes: BUC-21/g- C_3N_4 reduced $Cr(VI)$ under simulated sunlight.

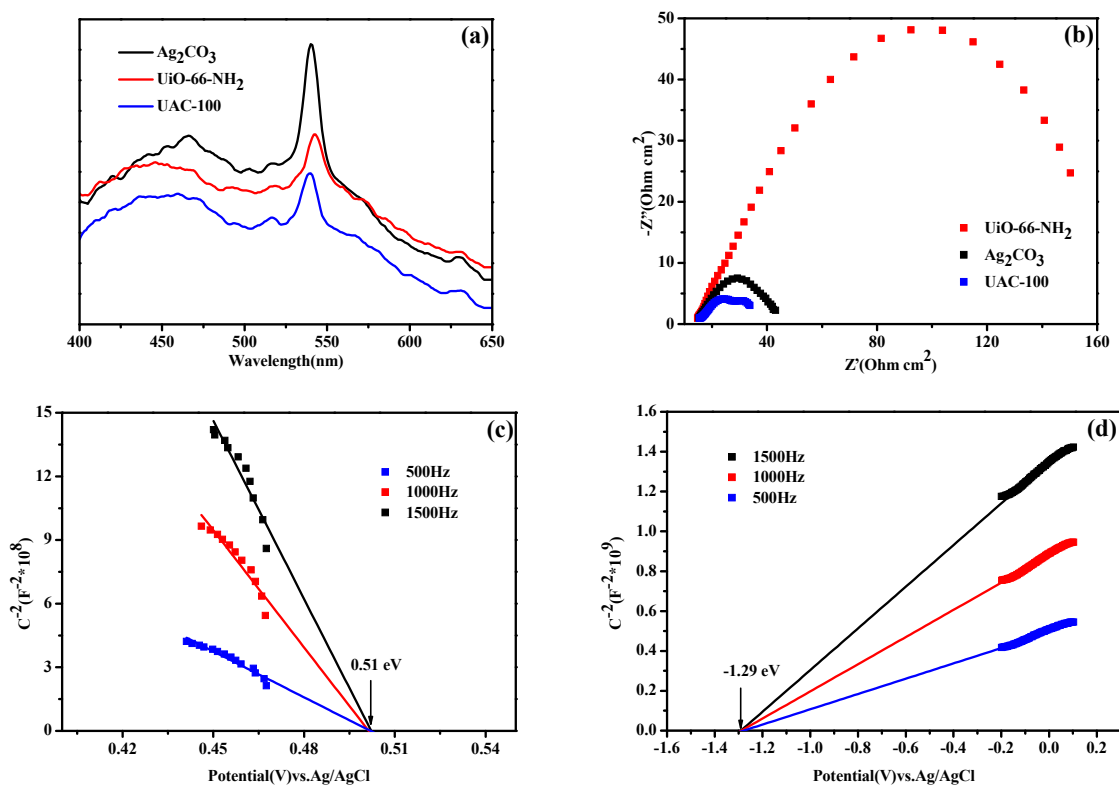
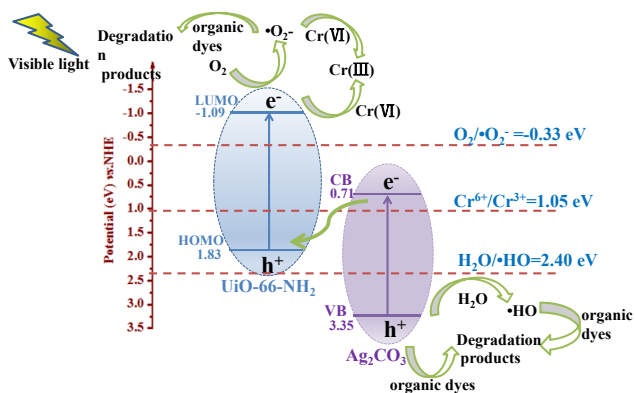


Fig. 10. (a) Photoluminescence spectra (PL) and (b) electrochemical impedance spectra (EIS); The Mott-Schottky curves of (c) Ag₂CO₃ and (d) UiO-66-NH₂ at various frequencies.

E_{FB} in Mott-Schottky, the maximum occupied molecular orbital (HOMO) of UiO-66-NH₂ and VB of Ag₂CO₃ were 1.83 eV and 3.35 eV vs NHE at pH = 7.0, respectively.

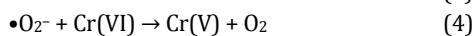
Based on the properties and experimental studies of the UAC-100 composite, UiO-66-NH₂, and Ag₂CO₃, the possible direct Z-scheme photocatalytic mechanism of organic dyes and Cr(VI) reduction under the irradiation of visible light was proposed (Scheme 2) [68–72]. Under the visible light irradiation, the electrons in the highest occupied molecular orbital (HOMO) of UiO-66-NH₂ will be excited to the lowest occupied molecular orbital (LUMO), and similarly, the electrons in the VB position of Ag₂CO₃ will be excited to the CB position. Considering that

the formation of UiO-66-NH₂/Ag₂CO₃ (UAC-100), the photo-induced electrons can be transferred from the CB of Ag₂CO₃ to consume the h^+ formed over HOMO of UiO-66-NH₂, which effectively shorten the electron transfer distance and facilitate the separation of electron-hole formed on the individual UiO-66-NH₂ and Ag₂CO₃. The $\bullet\text{O}_2^-$ is a key active substance that exhibits direct oxidative degradation of organic dyes, which can be generated as the LUMO value of UiO-66-NH₂ is -1.29 eV vs NHE, much more negative than the standard redox potential $E(\text{O}_2/\bullet\text{O}_2^-)$ (-0.33 eV vs NHE) [64]. At the same time, $\text{O}_2\cdot^-$ will also participate in the photocatalytic Cr(VI) reduction via Eqs. (3) and (4) [73,74], which can be demonstrated by the inhibition of Cr(VI) reduction in nitrogen atmosphere compared to normal indoor environments under the same conditions, as shown in Fig. S13. It is worth noting that the electrons generated on the LUMO of UiO-66-NH₂ will also directly participate in the Cr(VI) reduction because of the strong ability of Cr(VI) to capture electrons in the photocatalytic reduction of Cr(VI) to avoid the photo-corrosion of Ag₂CO₃, which can be proved from the integrity of the material before and after four cycles and XPS spectrum before and after photocatalytic Cr(VI) reduction (Fig. 9b and Fig. S11). Subsequently, the holes on the VB of Ag₂CO₃ can directly oxidize organic dyes and also oxidize the H₂O or $-\text{OH}$ molecules to form $\bullet\text{OH}$, which then participates in the photocatalytic degradation of organic dyes, because the VB potential (3.35 eV vs NHE) is greater than the H₂O/HO \cdot potential (2.40 eV vs NHE) [64]. The photocatalytic mechanism of the UAC-X composites shows that photo-induced holes are also



Scheme 2. The proposed Z-scheme mechanism for the photocatalytic Cr(VI) reduction and organic pollutant degradation over UAC-100 under visible light.

contributors to the degradation process of organic dyes. In the oxidation-reduction reaction of the UAC-X composites, the effective separation of holes and photo-induced electrons in the formed Z-scheme heterojunction contributes to the improved photocatalytic performance.



4. Conclusions

The UAC-X heterojunction with enhanced photocatalytic properties was successfully prepared by a simple ion-exchange-solution method. The morphology and structure of the UAC-X composites were characterized by FTIR, PXRD, SEM, TEM, HRTEM, UV-Vis DRS, and XPS. The photocatalytic activity of the UAC-X composites for Cr(VI) reduction is better than that of pure Ag_2CO_3 and UiO-66- NH_2 under visible light irradiation. Especially for UAC-100, the ideal effect can be achieved with less UiO-66- NH_2 dosage. PL analysis, electrochemistry measurement, capture of active substances, and ESR spectra demonstrated that the reduction enhancement of Cr(VI) is due to the faster separation of photo-induced electrons and holes and the reduction of $\cdot\text{O}_2^-$ over the interface of Z-scheme heterostructure. The effects of pH value, foreign ions, and small organic acids on the reduction of Cr(VI) and the organic dye oxidation properties of UAC-100 were also investigated. The presence of organic matters in the reaction system can enhance the photocatalytic Cr(VI) reduction performance. In addition, UAC-100 exhibits excellent photocatalytic oxida-

tion properties for RhB, MO, CR, and MB due to the generation of h^+ , $\cdot\text{HO}$, and $\cdot\text{O}_2^-$ with oxidizing properties under visible light. It is worth noting that UAC-100 had excellent reusability and stability in the experiment of photocatalytic reduction of Cr(VI). This work showed that the combination of UiO-66- NH_2 and Ag_2CO_3 can enhance the photocatalytic efficiency, which might be used in water treatment. We will carry out further work to address the photo-corrosion of Ag_2CO_3 , especially during the oxidative degradation toward organic pollutants.

Acknowledgments

This work was supported by the National Natural Science Foundation of China (51878023, 51578034), Great Wall Scholars Training Program Project of Beijing Municipality Universities (CIT&TCD20180323), Project of Construction of Innovation Teams and Teacher Career Development for Universities and Colleges Under Beijing Municipality (IDHT20170508), Beijing Talent Project (2018A35), and BUCEA Post Graduate Innovation Project (PG2019039).

References

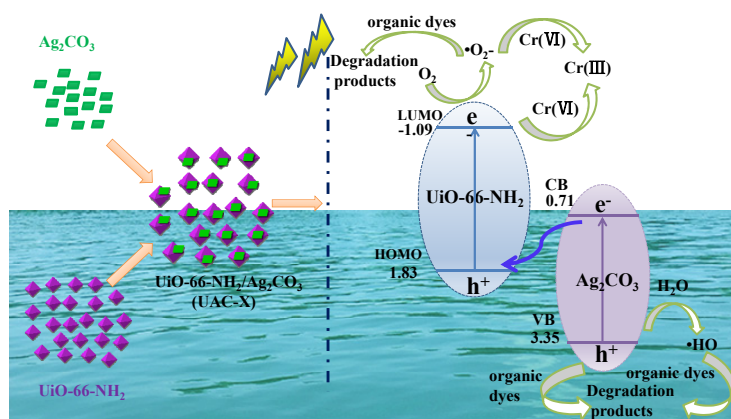
- [1] H. Dong, J. Deng, Y. Xie, C. Zhang, Z. Jiang, Y. Cheng, K. Hou, G. Zeng, *J. Hazard. Mater.*, **2017**, 332, 79–86.
- [2] W. Huang, N. Liu, X. Zhang, M. Wu, L. Tang, *Appl. Surf. Sci.*, **2017**, 425, 107–116.
- [3] J. J. Testa, M. A. A. Grela, M. I. Litter, *Environ. Sci. Technol.*, **2004**, 38, 1589–1594.
- [4] Y. Zhang, M. Xu, H. Li, H. Ge, Z. Bian, *Appl. Catal. B*, **2018**, 226,

Graphical Abstract

Chin. J. Catal., 2019, 40: 1912–1923 doi: S1872-2067(19)63433-9

Facile fabrication and enhanced photocatalytic performance of visible light responsive UiO-66- NH_2 / Ag_2CO_3 composite

Yun-Cai Zhou, Xue-Yan Xu, Peng Wang, Huifen Fu, Chen Zhao, Chong-Chen Wang *
Beijing University of Civil Engineering and Architecture



The UiO-66- NH_2 / Ag_2CO_3 composite (UAC-X) displayed outstanding photocatalytic activity due to the effective separation of photo-induced electrons and holes over the composite, which was contributed to the formed direct Z-scheme heterojunctions.

- 213–219.
- [5] Y. Xing, X. Chen, D. Wang, *Environ. Sci. Technol.*, **2007**, 41, 1439–1443.
 - [6] B. Galan, D. Castaneda, I. Ortiz, *Water Res.*, **2005**, 39, 4317–4324.
 - [7] C. Lei, X. Zhu, B. Zhu, C. Jiang, Y. Le, J. Yu, *J. Hazard. Mater.*, **2017**, 321, 801–811.
 - [8] G. Pugazhenth, S. Sachan, N. Kishore, A. Kumar, *J. Membr. Sci.*, **2005**, 254, 229–239.
 - [9] I. Heidmann, W. Calmano, *J. Hazard. Mater.*, **2008**, 152, 934–941.
 - [10] R. Liang, F. Jing, L. Shen, N. Qin, L. Wu, *J. Hazard. Mater.*, **2015**, 287, 364–372.
 - [11] L. B. Khalil, W. E. Mourad, M. W. Rophael, *Appl. Catal. B*, **1998**, 17, 267–273.
 - [12] C.E. Barrera-Diaz, V. Lugo-Lugo, B. Bilyeu, *J. Hazard. Mater.*, **2012**, 223–224, 1–12.
 - [13] H. Zhao, Q. Xia, H. Xing, D. Chen, H. Wang, *ACS Sustain. Chem. Eng.*, **2017**, 5, 4449–4456.
 - [14] V. Vaiano, O. Sacco, D. Sannino, P. Ciambelli, *Appl. Catal. B*, **2015**, 170–171, 153–161.
 - [15] Z. Wu, X. Yuan, J. Zhang, H. Wang, L. Jiang, G. Zeng, *ChemCatChem*, **2017**, 9, 41–64.
 - [16] Z. Sha, H. S. Chan, J. Wu, *J. Hazard. Mater.*, **2015**, 299, 132–140.
 - [17] H. Wang, X. Yuan, Y. Wu, G. Zeng, X. Chen, L. Leng, Z. Wu, L. Jiang, H. Li, *J. Hazard. Mater.*, **2015**, 286, 187–194.
 - [18] C. Chen, W. Ma, J. Zhao, *Chem. Soc. Rev.*, **2010**, 39, 4206–4219.
 - [19] H. Wang, L. Zhang, Z. Chen, J. Hu, S. Li, Z. Wang, J. Liu, X. Wang, *Chem. Soc. Rev.*, **2014**, 43, 5234–5244.
 - [20] J. Schneider, M. Matsuoka, M. Takeuchi, J. Zhang, Y. Horiuchi, M. Anpo, D.W. Bahnemann, *Chem. Rev.*, **2014**, 114, 9919–9986.
 - [21] C. Yu, Q. Fan, Y. Xie, J. Chen, Q. Shu, J. C. Yu, *J. Hazard. Mater.*, **2012**, 237–238, 38–45.
 - [22] Q. Xiang, J. Yu, M. Jaroniec, *J. Am. Chem. Soc.*, **2012**, 134, 6575–6578.
 - [23] Y. Feng, H. Li, L. Ling, S. Yan, D. Pan, H. Ge, H. Li, Z. Bian, *Environ. Sci. Technol.*, **2018**, 52, 7842–7848.
 - [24] H. Ye, Y. Liu, S. Chen, H. Wang, Z. Liu, Z. Wu, *Chin. J. Catal.*, **2019**, 40, 631–637.
 - [25] Y. Feng, L. Ling, J. Nie, K. Han, X. Chen, Z. Bian, H. Li, Z. L. Wang, *ACS Nano*, **2017**, 11, 12411–12418.
 - [26] C. Yu, L. Wei, J. Chen, Y. Xie, W. Zhou, Q. Fan, *Ind. Eng. Chem. Res.*, **2014**, 53, 5759–5766.
 - [27] C. Yu, G. Li, S. Kumar, K. Yang, R. Jin, *Adv. Mater.*, **2014**, 26, 892–898.
 - [28] S. Song, B. Cheng, N. Wu, A. Meng, S. Cao, J. Yu, *Appl. Catal. B*, **2016**, 181, 71–78.
 - [29] S. Li, X. Wang, Q. He, Q. Chen, Y. Xu, H. Yang, M. Lü, F. Wei, X. Liu, *Chin. J. Catal.*, **2016**, 37, 367–377.
 - [30] H. Yu, W. Chen, X. Wang, Y. Xu, J. Yu, *Appl. Catal. B*, **2016**, 187, 163–170.
 - [31] C. Dong, K.-L. Wu, X.-W. Wei, X.-Z. Li, L. Liu, T.-H. Ding, J. Wang, Y. Ye, *CrystEngComm*, **2014**, 16, 730–736.
 - [32] J. Meng, Q. Chen, J. Lu, H. Liu, *ACS Appl. Mater. Interfaces*, **2019**, 11, 550–562.
 - [33] A. Crake, K. C. Christoforidis, A. Kafizas, S. Zafeiratos, C. Petit, *Appl. Catal. B*, **2017**, 210, 131–140.
 - [34] Y. Su, Z. Zhang, H. Liu, Y. Wang, *Appl. Catal. B*, **2017**, 200, 448–457.
 - [35] R. Wang, L. Gu, J. Zhou, X. Liu, F. Teng, C. Li, Y. Shen, Y. Yuan, *Adv. Mater. Interfaces*, **2015**, 2, 1500037.
 - [36] C. Gomes Silva, I. Luz, F. X. Llabres i Xamena, A. Corma, H. Garcia, *Chem.-Eur. J.*, **2010**, 16, 11133–11138.
 - [37] L. Shi, X. Meng, T. Wang, H. Zhang, K. Chang, H. Liu, J. Ye, *Adv. Sci.*, **2015**, 2, 1500006.
 - [38] C.-C. Wang, X.-D. Du, J. Li, X.-X. Guo, P. Wang, J. Zhang, *Appl. Catal. B*, **2016**, 193, 198–216.
 - [39] X.-H. Yi, F.-X. Wang, X.-D. Du, P. Wang, C.-C. Wang, *Appl. Organomet. Chem.*, **2019**, 33, 1–11.
 - [40] L. Shen, S. Liang, W. Wu, R. Liang, L. Wu, *Dalton Trans.*, **2013**, 42, 13649–13657.
 - [41] Q. Xia, B. Huang, X. Yuan, H. Wang, Z. Wu, L. Jiang, T. Xiong, J. Zhang, G. Zeng, H. Wang, *J. Colloid Interface Sci.*, **2018**, 530, 481–492.
 - [42] C.-C. Wang, J.-R. Li, X.-L. Lv, Y.-Q. Zhang, G. Guo, *Energy Environ. Sci.*, **2014**, 7, 2831–2867.
 - [43] Q. Liang, M. Zhang, Z. Zhang, C. Liu, S. Xu, Z. Li, *J. Alloys Compd.*, **2017**, 690, 123–130.
 - [44] X.-H. Yi, F.-X. Wang, X.-D. Du, H. Fu, C.-C. Wang, *Polyhedron*, **2018**, 152, 216–224.
 - [45] H. Li, S. Yao, H.-L. Wu, J.-Y. Qu, Z.-M. Zhang, T.-B. Lu, W. Lin, E.-B. Wang, *Appl. Catal. B*, **2018**, 224, 46–52.
 - [46] D. Guo, R. Wen, M. Liu, H. Guo, J. Chen, W. Weng, *Appl. Organomet. Chem.*, **2015**, 29, 690–697.
 - [47] D. Azarifar, R. Ghorbani-Vaghei, S. Daliran, A. R. Oveisi, *ChemCatChem*, **2017**, 9, 1992–2000.
 - [48] J.-J. Zhou, R. Wang, X.-L. Liu, F.-M. Peng, C.-H. Li, F. Teng, Y.-P. Yuan, *Appl. Surf. Sci.*, **2015**, 346, 278–283.
 - [49] N. Zhang, X. Zhang, C. Gan, J. Zhang, Y. Liu, M. Zhou, C. Zhang, Y. Fang, *J. Photochem. Photobiol. A*, **2019**, 376, 305–315.
 - [50] X.-Y. Xu, C. Chu, H. Fu, X.-D. Du, P. Wang, W. Zheng, C.-C. Wang, *Chem. Eng. J.*, **2018**, 350, 436–444.
 - [51] X.-Y. Xu, J. Zhang, X. Zhao, H. Fu, C. Chu, P. Wang, C.-C. Wang, *ACS Appl. Nano Mater.*, **2019**, 2, 418–428.
 - [52] H. R. Abid, J. Shang, H.-M. Ang, S. Wang, *Int. J. Smart Nano Mater.*, **2013**, 4, 72–82.
 - [53] J. Yang, Y. Dai, X. Zhu, Z. Wang, Y. Li, Q. Zhuang, J. Shi, J. Gu, *J. Mater. Chem. A*, **2015**, 3, 7445–7452.
 - [54] Y. Ma, Z. Wang, X. Xu, J. Wang, *Chin. J. Catal.*, **2017**, 38, 1956–1969.
 - [55] J. Liu, B. Cheng, J. Yu, *Phys. Chem. Chem. Phys.*, **2016**, 18, 31175–31183.
 - [56] D. K. Padhi, K. Parida, *J. Mater. Chem. A*, **2014**, 2, 10300–10312.
 - [57] B. Sun, E. P. Reddy, P. G. Smirniotis, *Environ. Sci. Technol.*, **2005**, 39, 6251–6259.
 - [58] A. Liu, C. C. Wang, C. Z. Wang, H. F. Fu, W. Peng, Y. L. Cao, H. Y. Chu, A. F. Du, *J. Colloid Interface Sci.*, **2018**, 512, 730–739.
 - [59] X. Zhou, C. Hu, X. Hu, T. Peng, J. Qu, *J. Phys. Chem. C*, **2010**, 114, 2746–2750.
 - [60] N. Fiol, C. Escudero, I. Villaescusa, *Bioresource Technol.*, **2008**, 99, 5030–5036.
 - [61] L. Shen, R. Liang, M. Luo, F. Jing, L. Wu, *Phys. Chem. Chem. Phys.*, **2015**, 17, 117–121.
 - [62] L. Shen, W. Wu, R. Liang, R. Lin, L. Wu, *Nanoscale*, **2013**, 5, 9374–9382.
 - [63] L. Shen, L. Huang, S. Liang, R. Liang, N. Qin, L. Wu, *RSC Adv.*, **2014**, 4, 2546–2549.
 - [64] F. Chen, Q. Yang, Y. Wang, F. Yao, Y. Ma, X. Huang, X. Li, D. Wang, G. Zeng, H. Yu, *Chem. Eng. J.*, **2018**, 348, 157–170.
 - [65] M. Xu, Y. Chen, J. Qin, Y. Feng, W. Li, W. Chen, J. Zhu, H. Li, Z. Bian, *Environ. Sci. Technol.*, **2018**, 52, 13879–13886.
 - [66] K. He, J. Xie, X. Luo, J. Wen, S. Ma, X. Li, Y. Fang, X. Zhang, *Chin. J. Catal.*, **2017**, 38, 240–252.
 - [67] W. Fa, P. Wang, B. Yue, F. Yang, D. Li, Z. Zheng, *Chin. J. Catal.*, **2015**, 36, 2186–2193.
 - [68] Q. Liang, S. Cui, J. Jin, C. Liu, S. Xu, C. Yao, Z. Li, *Appl. Surf. Sci.*, **2018**, 456, 899–907.
 - [69] X. Li, J. Yu, M. Jaroniec, X. Chen, *Chem. Rev.*, **2019**, 119, 3962–4179.

- [70] K. Qi, B. Cheng, J. Yu, W. Ho, *Chin. J. Catal.*, **2017**, 38, 1936–1955.
- [71] X. Li, J. Xie, C. Jiang, J. Yu, P. Zhang, *Front. Environ. Sci. Eng.*, **2018**, 12, 1–32.
- [72] G. Gebreslassie, P. Bharali, U. Chandra, A. Sergawie, P. K. Baruah, M. R. Das, E. Alemayehu, *Appl. Organomet. Chem.*, **2019**, e5002.
- [73] J. C. Wang, J. Ren, H. C. Yao, L. Zhang, J. S. Wang, S. Q. Zang, L. F. Han, Z. J. Li, *J. Hazard. Mater.*, **2016**, 311, 11–19.
- [74] X. Hu, H. Ji, F. Chang, Y. Luo, *Catal. Today*, **2014**, 224, 34–40.

UiO-66-NH₂/Ag₂CO₃复合物简易制备及其在可见光驱动下的高效光催化性能

周云彩, 徐雪艳, 王 鹏, 付会芬, 赵 晨, 王崇臣*

北京建筑大学建筑结构与环境修复功能材料北京重点实验室, 北京100044

摘要:近年来, 金属-有机骨架(MOFs)作为一种多相光催化剂被越来越多地应用于光催化分解水制氢、还原CO₂、还原Cr(VI)和降解环境有机污染物。尽管MOFs在光催化领域表现优异, 但是仍然面临一些问题, 例如多数MOFs材料仅在紫外线激发下才能表现出光催化活性, 多数MOFs材料导电性不高、水稳定性欠佳及光生电子和空穴容易复合等。为此, 与一些窄带隙半导体光催化剂构建复合物是增强MOFs光催化性能的一个有效策略。

本文采用简单的原位离子交换沉积法, 以UiO-66-NH₂和AgNO₃为前驱体在室温下快速制备了一系列具直接Z型异质结的UiO-66-NH₂/Ag₂CO₃复合物(记为UAC-X, 其中X=20、50、100、150和200, 代表UiO-66-NH₂在复合物中的含量)。采用傅里叶变换红外光谱(FTIR)、粉末X射线衍射(PXRD)、扫描电镜(SEM)、透射电镜(TEM)、高倍透射电镜(HRTEM)、紫外-可见漫反射(UV-Vis DRS)和X射线光电子能谱(XPS)等技术对UAC-X复合物的形貌和结构进行了表征。研究了UAC-X在可见光照射下光催化还原六价铬(Cr(VI))和UAC-100降解有机染料的性能。探究了不同pH (pH = 2、3、4、6和8)、不同小分子有机酸(柠檬酸、酒石酸和草酸)及共存离子(自来水和地表水中的离子)对光催化还原Cr(VI)的影响。

结果表明, PXRD谱图显示UAC-X的衍射峰位置分别与UiO-66-NH₂和Ag₂CO₃峰位置完全吻合。SEM、TEM和HRTEM图片证明在UAC-X复合物中Ag₂CO₃附着在UiO-66-NH₂表面。光照50 min后, UAC-X复合物还原Cr(VI)的效率(UAC-20和UAC-50分别为68%和86%, UAC-100、UAC-150和UAC-200为100%)均高于UiO-66-NH₂(19%)和Ag₂CO₃(8.0%)。UAC-X复合物中UiO-66-NH₂含量增加(比如UAC-20、UAC-50和UAC-100)导致其光催化Cr(VI)活性增强, 其原因在于比表面积增大, 且表面增强的正电荷对Cr₂O₇²⁻吸附能力增强, 最终提升了其光催化效率。

不同pH值下的光催化实验结果表明: 酸性条件下光催化效率远优于碱性条件, 这是因为在酸性条件下充足的H⁺和表面正电性有利于Cr(VI)还原为Cr(III); 在碱性条件下, UAC-100表面呈负电性与CrO₄²⁻发生排斥, 且形成的Cr(OH)₃沉淀会遮盖催化剂表面活性位点, 导致光催化效率下降。反应溶液中的共存离子也会影响光催化效率: 自来水中的无机离子可在一定程度上抑制UAC-100对Cr(VI)的光催化效率; 湖水中存在的少量有机物可消耗空穴而减弱共存无机离子对Cr(VI)还原效率的负面影响。向无共存离子存在的模拟废水体系中加入酒石酸、柠檬酸和草酸等小分子有机酸时, UAC-100作为光催化剂还原Cr(VI)的速率和效率显著提高, 这是因为小分子有机物可有效捕捉空穴, 加强光生电子和空穴的分离。光致发光分析、电化学分析、电子自旋共振(ESR)和活性物质捕获实验显示, UAC-100中Ag₂CO₃导带(CB)上的光生电子转移至UiO-66-NH₂最高已占轨道(HOMO), 表明在UAC-100复合物中形成了直接Z型异质结, 提高了光生电子和空穴的分离效率, 最终加强了光催化还原Cr(VI)的活性。同时, UAC-100经过4次光催化循环实验后其还原Cr(VI)效率仍然可达99%, 且PXRD谱图未见明显变化, 表明UAC-100具有稳定性和重复利用性。综上, UiO-66-NH₂/Ag₂CO₃是一种具有应用前景的高效复合型光催化剂。

关键词: 金属-有机骨架; 碳酸银; 六价铬; 光催化; 反应机理

收稿日期: 2019-05-01. 接受日期: 2019-06-26. 出版日期: 2019-12-05.

*通讯联系人. 电话/传真: (010)61209186; 电子信箱: wangchongchen@bucea.edu.cn

基金来源: 国家自然科学基金(51878023, 51578034); 北京市属高等学校长城学者培养计划(CIT&TCD20180323); 北京市属高等学校创新团队建设与教师职业发展计划(IDHT20170508); 北京市百千万人才工程(2018A35); 北京建筑大学研究生创新项目(PG2019039).

本文的电子版全文由Elsevier出版社在ScienceDirect上出版(<http://www.sciencedirect.com/science/journal/18722067>).